Editors' Suggestion

Programmable Spatiotemporal Quantum Parametric Mode Sorter

Malvika Garikapati,[1,2,‡] Santosh Kumar,[1,2,*,‡] He Zhang,[1,2] Yong Meng Sua,[1,2] and Yu-Ping Huang[1,2,†]

[1] *Department of Physics, Stevens Institute of Technology, Hoboken, New Jersey 07030, USA*
[2] *Center for Quantum Science and Engineering, Stevens Institute of Technology, Hoboken, New Jersey 07030, USA*

(Received 9 January 2023; accepted 14 March 2023; published 24 April 2023)

We experimentally demonstrate a programmable parametric mode sorter of high-dimensional signals in a composite spatiotemporal Hilbert space through mode-selective quantum frequency up-conversion. As a concrete example and with quantum communication applications in mind, we consider the Laguerre-Gaussian and Hermite-Gaussian modes as the spatial and temporal state basis for the signals, respectively. By modulating the spatiotemporal profiles of the up-conversion pump, we demonstrate the faithful selection of signal photons in those modes and their superposition modes. Our results show an improvement in the quantum mode-sorting performance by coupling the up-converted light into a single-mode fiber and/or operating the up-conversion at the edge of phase matching. Optimizing pump temporal profiles allows us to achieve more than 12-dB extinction for mutually unbiased basis (MUB) sets of the spatiotemporal modes. This fully programmable and efficient system could be a viable resource for quantum communications, quantum computation, and quantum metrology.

DOI: 10.1103/PhysRevApplied.19.044070

I. INTRODUCTION

Nowadays, quantum parametric frequency-conversion processes such as spontaneous parametric down-conversion [1–3], second-harmonic generation [4], sum- and difference-frequency generation, and four-wave mixing [5] are extensively utilized in quantum optics [6–8], with applications in hybrid quantum networks [9,10], creating entanglement between disparate quantum memories [11,12], realizing low-noise infrared up-conversion photon counters [13–15], and so on. Meanwhile, quantum systems subtending high-dimensional (HD) Hilbert spaces have been studied due to their advantages in a higher information capacity, enhanced security, or increased resistance to noise. Thus far, higher-dimensional information coding has been demonstrated on various platforms such as those of trapped ions [16], polar molecules [17], Rydberg atoms, cold atomic ensembles [18], photonic systems, or superconducting phase qudit [19]. In photonic systems, the information can be encoded in a HD Hilbert space with multiple degrees of freedom (DOF) over polarization, spatial, time, energy, and optical path [20–26]. This multiple DOF of the photons can be coherently coupled with each other to boost quantum communication capabilities [27] with broad applications in quantum key distribution [28,29], quantum logic operations, quantum teleportation, quantum metrology [30–32], and so on.

A challenge to HD quantum information processing is with efficient sorting and processing of the highly multiplexed modes. Indeed, several techniques have been demonstrated to sort the spectral modes by using linear-optical resonators [33,34], and sort the spatial [35–40] and temporal [28,41–43] modes, respectively, by using nonlinear optics. Among them, those nonlinear-optical techniques have the upper hand in mode sorting as compared to their linear counterparts, as they can manipulate single photons in a single step (i.e., by singly passing through a nonlinear waveguide) and, in principle, without any loss. The same techniques will allow nearly lossless modulation of quantum signals [44], enabling networked quantum applications over heterogeneous material platforms.

While most of the above work has focused on sorting either spatial or temporal modes, the ability to sort combined spatial-temporal (ST) modes could find vast applications in developing practical quantum technologies [23,26,45–47]. Recently, we demonstrated a HD quantum system by combining spatial and temporal DOF by using a spatial light modulator (SLM) and optical delay line (ODL), respectively [48]. There, we demonstrated efficient mode sorting by selectively up-converting signal modes with spatially modulated and temporally delayed pumps. It has a limited capacity due to the delay-only temporal control of the Gaussian pulses, which restricts its

*skumar5@stevens.edu
†yhuang5@stevens.edu
‡These two authors contributed equally.

advantage for HD Hilbert-space quantum communication and computation.

In this paper, we overcome the aforementioned restriction of our previous study by adding arbitrary temporal modulation and demonstrating HD quantum parametric mode sorting (QPMS) over the compound ST Hilbert space with arbitrarily reconfigurable modes. Specifically, we utilize spatial light modulators for controlling spatial DOF [48,49] and an optical arbitrary waveform generator (OAWG) based on spectral line-by-line pulse shaping to manipulate the amplitude and phase profiles of the time-frequency DOF [42,50,51]. We experimentally demonstrate that the mutually unbiased basis (MUB) in a HD Hilbert space can be selectively up-converted according to their spatial and/or time-frequency tomography. This allows photon-efficient applications over overlapping yet orthogonal spatial and temporal modes, thus accessing a much larger Hilbert space than allowed by each individual DOF [21,46,52]. This also helps achieve high selectivity by merging the spatial and time-frequency modes, reducing error probabilities in HD quantum applications. This efficient programmable manipulation of HD ST modes could find practical applications in emerging quantum technologies, including robust HD quantum key distribution.

II. MODEL

We consider photons in ST modes $\Psi = E_r(x,y)E_t(t)$, where $E_r(x,y)$ and $E_t(t)$ are the electric fields in the spatial and temporal domains, respectively. We exploit a HD Hilbert space by preparing quantum states in Laguerre-Gaussian (LG) spatial mode basis and Hermite-Gaussian (HG) temporal basis. To retrieve relevant quantum information, we need to extract the desired mode among a plethora of modes generated by processes like spontaneous four-wave mixing [5,53,54], multimode spontaneous parametric down-conversion [46,55,56], and antibunching photon emission in quantum dots [57,58]. We present a QPMS scheme that is realized through sum-frequency (SF) generation in a second-order χ^2 nonlinear crystal described by a set of coupled differential equations (see Ref. [48] for details). In our current setup, we use pump and signal input pulses having similar wavelengths under the undepleted pump approximation where the inverse group-velocity mismatch between them can be neglected so that our system operates in the single sideband velocity-mismatch (SSVM) regime [43,56]. When the temporal pulse width of the pump is smaller than the temporal walkoff between the pump and SF pulses in the crystal, high-mode selectivity can be achieved. We numerically simulate the results using an adaptive split-step Fourier method under the slowly varying envelope approximation. For both simulation and experiment discussions, we define the selectivity (S) of the signal quantum state for each pump state as

$$S = 10\log_{10}\left(\frac{N_D}{\sum_{i\neq D} N_i}\right), \tag{1}$$

where N_D is the number of SF photons in the "desired" mode among the other considered modes, as measured using the Si avalanche photodiode (Si APD). Figure 1 shows a schematic of our QPMS system that can selectively up-convert the desired signal mode among overlapping LG spatial modes and HG temporal modes by passing it through a nonlinear crystal with a specifically designed ST pump.

In this paper, we exclusively consider spatiotemporal modes, where spatial modes are defined as $|X_l^{p,s}\rangle$ with LG orbital angular momentum 'l'($\equiv 0, \pm1, \pm2,\dots$), and temporal modes are defined as $|T_m^{p,s}\rangle$ with HG higher-order mode index 'm' ($\equiv 0,1,2,\dots$). Here, 'p' stands for the pump, and 's' stands for the signal. For simplicity, we consider that the information is stored in a unique quantum state among three HG temporal modes $|T_0\rangle$, $|T_1\rangle$, $|T_2\rangle$ and five LG spatial modes $|X_{-2}\rangle$, $|X_{-1}\rangle$, $|X_0\rangle$, $|X_1\rangle$, $|X_2\rangle$. To selectively up-convert the signal photons in each of these 15 ST modes, we use a pump with a unique ST mode profile. We monitor and analyze the SF output for each of the 225 pairs of the ST pump and signal modes.

To thoroughly understand our hybrid system, we first independently illustrate the outcome of spatial and temporal processes. In Fig. 1(i), we prepare spatial and temporal quantum states for the signal. In Fig. 1(ii), we prepare pump states with different temporal modes and a constant spatial mode. We employ a Gaussian configuration for the spatial DOF to achieve maximum conversion efficiency and clearly recognize the features of the temporal DOF. Similarly, in Fig. 1(iii), we prepare different spatial modes by maintaining a constant temporal mode with a Gaussian profile. Figure 1(iv) represents the simulated SF outcome for a combination of these states. It is constructed by combining specific $|T_{1,2,3}\rangle$ modes for both pump and signal and calculating the SF output at the different delays. We consider the SF counts at zero delays to estimate the SF counts at the central overlap accurately. We observe high SF counts along the diagonal elements, which correspond to identical pump and signal temporal modes as $|T_0^p, T_0^s\rangle$, $|T_1^p, T_1^s\rangle$, and $|T_2^p, T_2^s\rangle$. The off-diagonal elements correspond to SF generation for pump and signal with orthogonal temporal modes like $|T_0^p, T_1^s\rangle$, $|T_0^p, T_2^s\rangle$, $|T_1^p, T_0^s\rangle$, $|T_1^p, T_2^s\rangle$, $|T_2^p, T_0^s\rangle$, and $|T_2^p, T_1^s\rangle$. These modes show significantly lower SF output at zero delays. The spectral profiles of the 2-ps signal and pump temporal pulses are shown in Appendix A. We plot the intensity and shape of the output SF pulses in Fig. 1(v) by simulating spatial $|X_i\rangle$ modes for both input pulses and calculating the output at each spatial location after passing it through the same

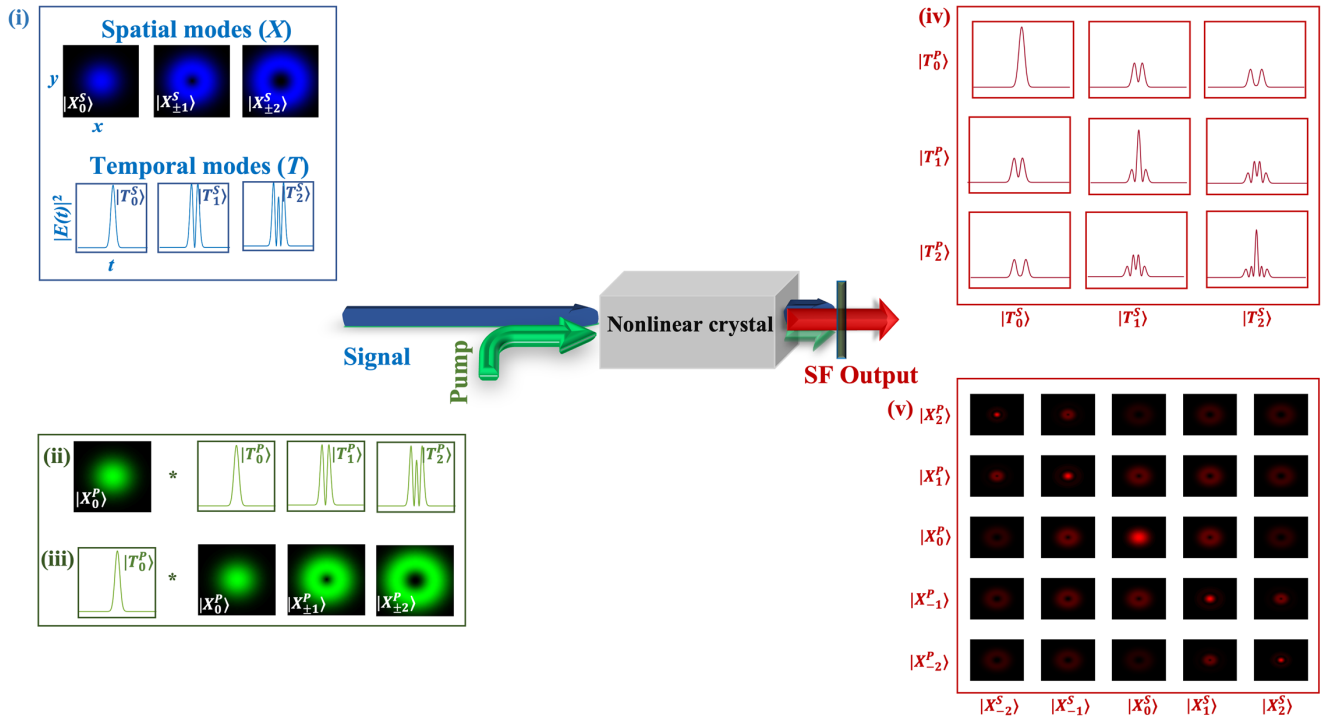

FIG. 1. Schematic of ST quantum parametric mode sorter using a χ^2 nonlinear crystal with signal (blue), pump (green), and SF output (red). (i) represents the signal states with spatial ($X^S_{i=0,\pm1,\pm2}$) and temporal ($T^S_{i=0,1,2}$) modes. (ii) A set of pump states with a Gaussian spatial mode $|X^p_0\rangle$ and different temporal modes $|T^p_0\rangle$, $|T^p_1\rangle$, and $|T^p_2\rangle$. (iii) represents pump states with a Gaussian temporal mode $|T^p_0\rangle$ and different spatial modes $|X^p_{-2}\rangle$, $|X^p_{-1}\rangle$, $|X^p_0\rangle$, $|X^p_1\rangle$ and $|X^p_2\rangle$. (iv) SF temporal outputs when the signals are combined with the pumps of (ii). (v) The SF spatial outputs when the signals are combined with the pumps of (iii) at zero delay.

crystal. We observe higher intensity for the diagonal elements as compared to off-diagonal elements. Since the diagonal terms correspond to pump mode $|X^p_i\rangle$, which efficiently up-converts signal modes $|X^s_{-i}\rangle$ [38]. As Appendix B shows, we also experimentally capture these spatial SF output modes on a CCD camera.

We further optimize the pump temporally using particle swarm optimization (PSO) to achieve better fidelity in selecting the desired signal. Likewise, we use this technique to simulate the arbitrary shape of the pump according to the experimental condition (as discussed in the next section). Here, we iteratively optimize the selectivity by individually manipulating the relative phase of 37 evenly spaced frequency comb lines simultaneously on an ensemble of 16 potential candidates (C). The phase change of each comb line in a particular candidate is influenced by its last known phase, its best-known phase (personal best), and the best-known phase of the entire ensemble (global best) with an adaptively changing weight component as shown below:

$$C_n^{(i+1)} = w * C_n^{(i)} + w_p * R_1 * C_{\mathrm{PB}}^{(i)} + w_g * R_2 * C_{\mathrm{GB}}^{(i)}, \quad (2)$$

where w, w_p, and w_g are the adaptively selected weight parameters, $C_{\mathrm{PB}}^{(i)}$ and $C_{\mathrm{GB}}^{(i)}$ are the personal and global best candidates achieved up to the ith iteration. R_1 and R_2 are randomly generated weight parameters added to utilize the search space intelligently. We can similarly optimize the pump in the spatial domain to further improve the selectivity, as discussed in our previous work [49].

III. EXPERIMENTAL SETUP

Figure 2 shows a continuous-wave light from a tunable laser source (TLS) at the central wavelength, 1546.6 nm, is sent to the optical frequency comb generator (OFCG). We use a commercially available optical frequency comb generator (Optocomb, WTEC-01-25). It consists of a phase modulator in a Fabry-Perot cavity driven by a 25-GHz radiofrequency signal and generates a phase-coherent broadband frequency comb with a line spacing 25 GHz. The output of the OFCG is low (approximately −20 dBm), which is then amplified by erbium-doped fiber amplifiers (EDFAs). The amplified comb lines are manipulated individually (line-by-line) in amplitude and phase by the waveshaper (Finisar 16000A) for optical arbitrary waveform generation [42,51]. This can be controlled by a MATLAB-based interface that observes the output by using an optical spectrum analyzer (OSA). The waveshaper provides pump (1551 nm) and signal (1559 nm)

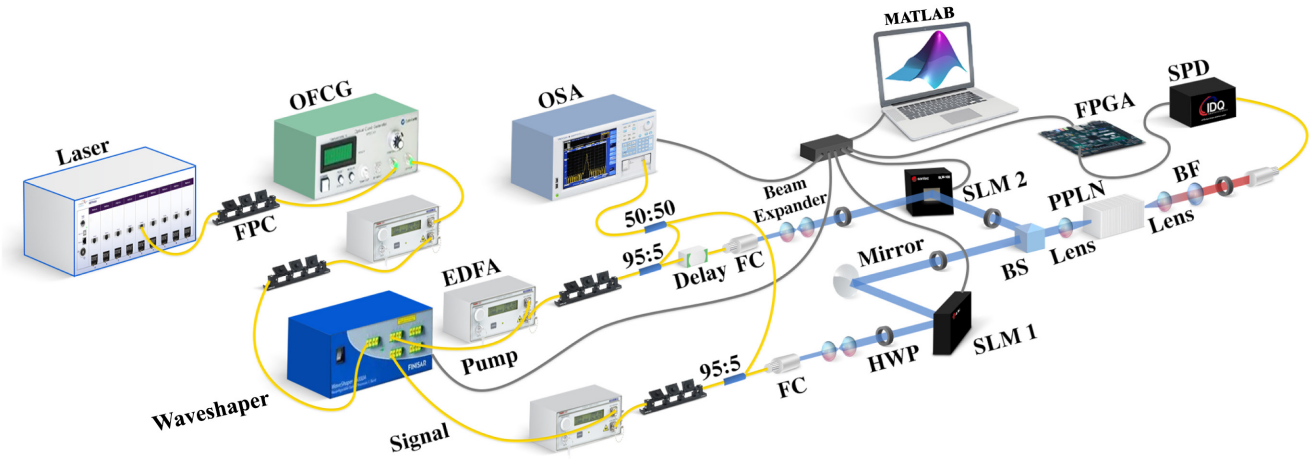

FIG. 2. Experimental setup for the programmable quantum parametric mode sorter in the ST domain. OFCG, optical frequency-comb generator; EDFA, erbium-doped fiber amplifier; FPC, fiber polarization controller; OSA, optical spectrum analyzer; FC, free space to fiber coupler; HWP, half-wave plate; SLM, spatial light modulator; BS, beam splitter; PPLN, magnesium-doped periodic poled lithium niobate crystal; SPD, visible single-photon detector; BF, bandpass filter.

separately with designated temporal modes, verified via the frequency-resolved optical gating (FROG) method. The response time of the waveshaper is 500 ms. The pump and signal are further amplified by the two separated EDFAs to overcome the insertion loss approximately 4.5 dB of the waveshaper. An optical delay line (ODL) in the pump arm is used to scan the relative time delay of the pump and signal pulses. Then vertically polarized pump and signal pulses propagate in free space before being incident on two separate spatial-light modulators (Santec SLM-100, 1440 × 1050 pixels, pixel size 10 × 10 μm^2). The response time of both SLMs is 300 ms. We also add some free-space spectral filters to suppress the amplified spontaneous noise of the EDFA in the pump and signal arms. A beam splitter combines the signal and pump into the nonlinear crystal (5 mol % MgO-doped periodic poled lithium niobate crystal). We test two separate nonlinear crystals with lengths 1 and 2.5 cm, generating SF output photons with a normalized conversion efficiency of approximately 1%/W/cm^2. Temporal walkoffs between the pump and SF pulses for 1- and 2.5-cm-long crystals are 1.2 and 3 ps, respectively. The parasitic pump and the generated second harmonic of the pump are filtered out using two 850-nm-long pass filters (FELH850) and three 775-nm bandpass filters (FBH770-10), with 100- and 150-dB suppression, respectively. After that, the SF output is coupled into single-mode fiber and detected by a high-speed single-pixel silicon avalanche photodiode (ID100). Then, a time-to-digital converter (TDC) can digitally count the number of photons, and MATLAB can postprocess the data [38].

IV. RESULTS

Effect of crystal length on selectivity: due to limitations of the OFCG, the wavelengths of our pump and signal are only 8 nm apart. In this case, the inverse group-velocity mismatch between the pump and signal can be neglected, making our system operate in the SSVM regime [43]. High mode selectivity is achieved when the temporal width of the pump is within the temporal walkoff between the pump and SF pulses in the crystal, i.e., the pump's spectral bandwidth exceeds the phase-matching bandwidth of the crystal. We plot the phase-matching curve of the crystal by sweeping the wavelength and measuring the generated SF power at a constant temperature. By fitting this experimental phase-matching curve of the nonlinear crystal on top of an ideal sinc^2 curve, we evaluate the temporal walkoff between the pump and SF pulses in the 1- and 2.5-cm crystal to be 1.2 and 3 ps, respectively. In Table I, we show the selectivity results for temporally optimized and unoptimized pump pulses for the 1- and 2.5-cm crystals (only for two temporal signal modes with spatial Gaussian). We choose a temporal pulse width of 2 ps for both pump and signal pulses to show the relation between temporal walkoff and QPMS condition distinctly. We observe a larger selectivity for both $|T_0^p\rangle$ and $|T_1^p\rangle$ in

TABLE I. Experimentally evaluated mode selectivity [using Eq. (1)] between two signal modes $|T_0^s\rangle$ and $|T_1^s\rangle$ with 2-ps pulse width, temporally optimized and unoptimized pumps $|T_0^p\rangle$ and $|T_1^p\rangle$ for two different lengths of the crystals.

Pump mode	Crystal length 1 cm		Crystal length 2.5 cm	
	$\|T_0^s\rangle$ (dB)	$\|T_1^s\rangle$ (dB)	$\|T_0^s\rangle$ (dB)	$\|T_1^s\rangle$ (dB)
$\|T_0^p\rangle$	6.13	−6.13	11.17	−11.17
$\|T_1^p\rangle$	−4.48	4.48	−10.27	10.27
Optimized $\|T_0^p\rangle$	7.32	−7.32	16.09	−16.09
Optimized $\|T_1^p\rangle$	−5.46	5.46	−13.72	13.72

TABLE II. Experimentally evaluated temporal mode selectivity of the signal state $|T_0\rangle$, $|T_1\rangle$ and $|T_2\rangle$ with temporally optimized and unoptimized pump state $|T_0\rangle$, $|T_1\rangle$, and $|T_2\rangle$ for two different pulse widths (2 and 7 ps) in a 2.5-cm-long nonlinear crystal. The selectivity values for each pump mode are calculated using Eq. (1).

Pump mode	Pulse width (ps)	$\|T_0^s\rangle$ (dB)	$\|T_1^s\rangle$ (dB)	$\|T_2^s\rangle$ (dB)	Pulse width (ps)	$\|T_0^s\rangle$ (dB)	$\|T_1^s\rangle$ (dB)	$\|T_2^s\rangle$ (dB)
$\|T_0^p\rangle$	2	10.28	−11.24	−17.97	7	0.42	−8.34	−2.73
$\|T_1^p\rangle$	2	−10.96	5.71	−7.98	7	−3.75	3.06	−14.53
$\|T_2^p\rangle$	2	−6.5	−7.66	3.11	7	−9.06	−4.63	2.37
Optimized $\|T_0^p\rangle$	2	10.28	−16.39	−17.97	7	3.87	−13.93	−4.72
Optimized $\|T_1^p\rangle$	2	−14.31	7.28	−8.5	7	−4.50	2.69	−10.15
Optimized $\|T_2^p\rangle$	2	−21.43	−6.76	6.55	7	−8.74	−11.29	6.38

the 2.5-cm crystal as compared to the 1-cm crystal because 2 ps is smaller than the temporal walkoff between the pump and SF pulses in the 2.5-cm crystal. We also show a significant improvement in the selectivity for both temporal modes by employing an optimized pump pulse.

To achieve higher selectivity in a 1-cm crystal, we must use a temporal pulse width smaller than 1.2 ps. The spectral width of such a pulse is over 3 nm and spans near the peak of the phase matching for the second-harmonic generation process, which leads to higher Raman noise. To significantly reduce the Raman noise, we use a temporal pulse width of over 2 ps with a spectral bandwidth of 1.6 nm through a 2.5-cm crystal [43].

Effect of pulse width on temporal selectivity: in Table II, we show the selectivity results for 2- and 7-ps temporally optimized and unoptimized pump pulses with a constant spatial profile for both pump and signal as $|X_0^p, X_0^s\rangle$. In this case, 2 ps is less than the temporal walkoff between the pump and SF pulses in the crystal and yields higher selectivity than the 7-ps pulse. For instance, unoptimized mode $|T_0^p, T_0^s\rangle$ gives a $\sim$ 9.8 dB difference in selectivity between 2- and 7-ps pulses. Even after significantly improving

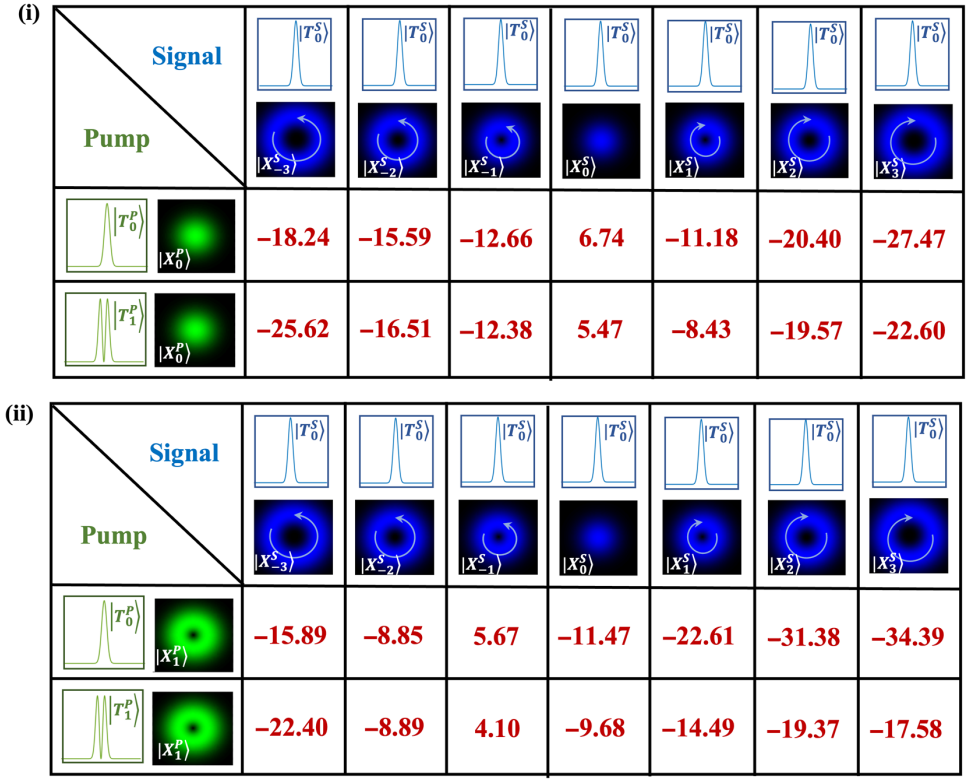

FIG. 3. Selectivity results in dB measured experimentally for five different signal spatial modes and $|T_0^s\rangle$ temporal mode [signal (blue), pump (green), and SF output (red)]. Each row represents the pump in two different temporal modes ($|T_0^p\rangle$, $|T_1^p\rangle$) with spatial mode $|X_0^p\rangle$ in (i) and $|X_0^p\rangle$ in (ii).

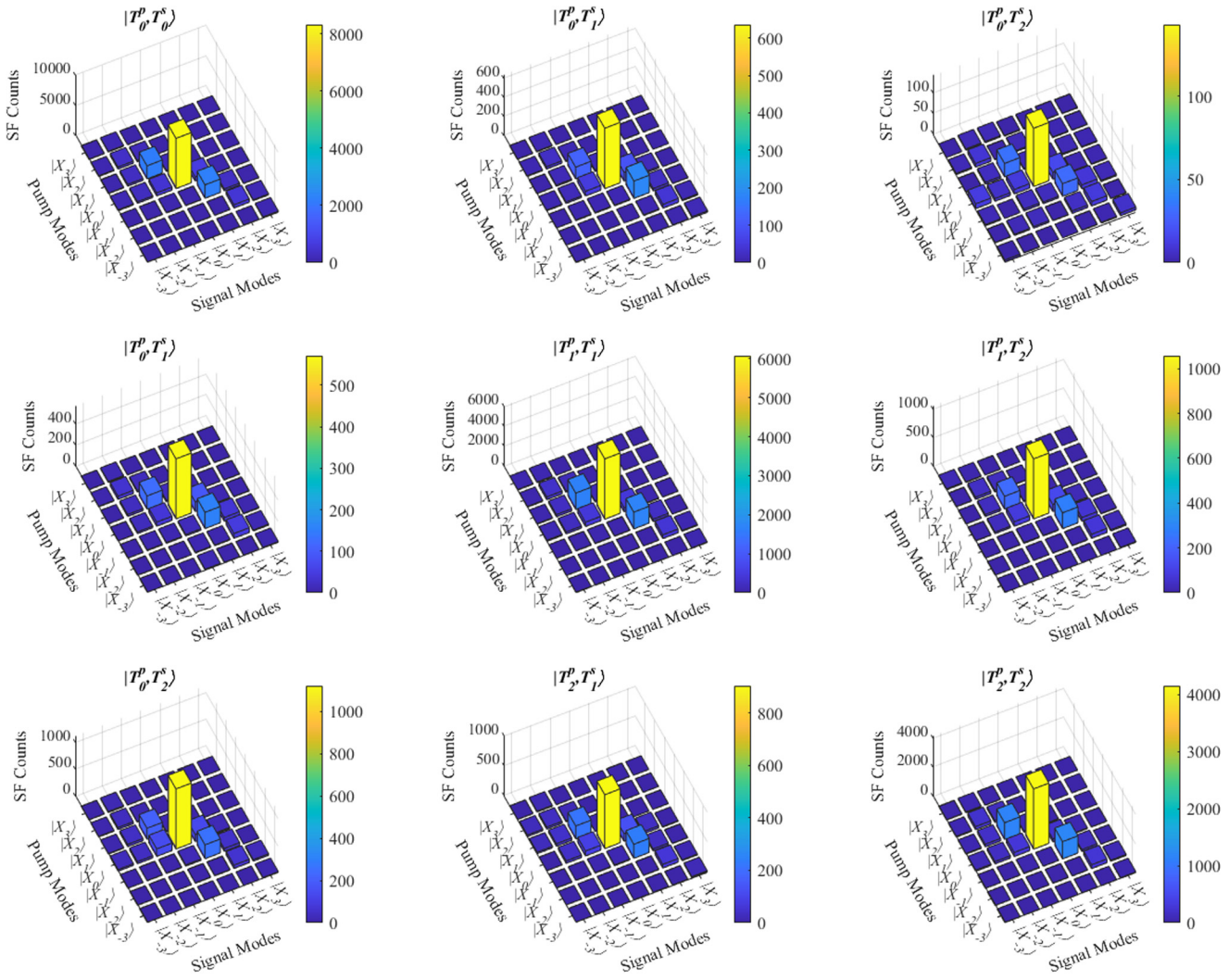

FIG. 4. Measured SF photon counts with different combinations of ST tomography. Here, each of the nine subfigures has a different combination of temporal HG pump and signal modes ($|T_0\rangle$, $|T_1\rangle$ and $|T_2\rangle$) with 2-ps pulse width. Each subfigure consists of SF count data corresponding to 25 combinations of spatial LG pump and signal modes ($|X_{-3}\rangle$, $|X_{-2}\rangle$, $|X_{-1}\rangle$, $|X_0\rangle$, $|X_1\rangle|X_2\rangle$,, and $|X_3\rangle$). The color bar in each subfigure represents the SF photon counts.

selectivity by utilizing optimized pump pulses, we can decrease only this to approximately 6.4 dB. In both cases, we observe that we can achieve high selectivity when the temporal shape of the pump and signal are identical $|T_0^p, T_0^s\rangle$, $|T_1^p, T_1^s\rangle$, and $|T_2^p, T_2^s\rangle$. $|T_0^p\rangle$ has a higher selectivity between $|T_1^s\rangle$ than $|T_2^s\rangle$, since $|T_0\rangle$ and $|T_2\rangle$ have a nonzero amplitude at zero delay. Our experimental results are on par with the theoretical simulations without the need for any fitting parameter. We also show how there is an abrupt drop in selectivity as the pulse width increases more than the temporal walkoff of the system in Appendix C.

Spatiotemporal mode selectivity: by combining spatial and temporal DOF, we take full advantage of the ST quantum states while being able to selectively up-convert a unique quantum state with high selectivity. Figure 3 demonstrates how we can use different ST pump profiles to selectively up-convert a unique ST signal mode among the seven modes considered. While $|X_0^p\rangle$ can efficiently up-convert a signal in $|X_0^s\rangle$ mode in Fig. 3(i), we also show that $|T_0^p\rangle$ can up-convert a signal in $|T_0^s\rangle$ with higher selectivity than $|T_1^p\rangle$. Figure 3(ii) shows similar results for pump mode, $|X_1^p\rangle$, which can up-convert signal mode $|X_{-1}^s\rangle$ with high selectivity when their temporal modes are $|T_0^p, T_0^s\rangle$. We observe an approximately 1.5 dB lower selectivity when the temporal profile of the pump and signal are not identical.

In Figs. 4 and 5, we show the tomography of spatial and temporal modes for 2- and 7-ps pulse width, respectively. Each of the nine subplots represents the SF output for a different pair of temporal modes for pump and signal, respectively. Each row represents a different pump mode, whereas the columns represent different signal modes. For

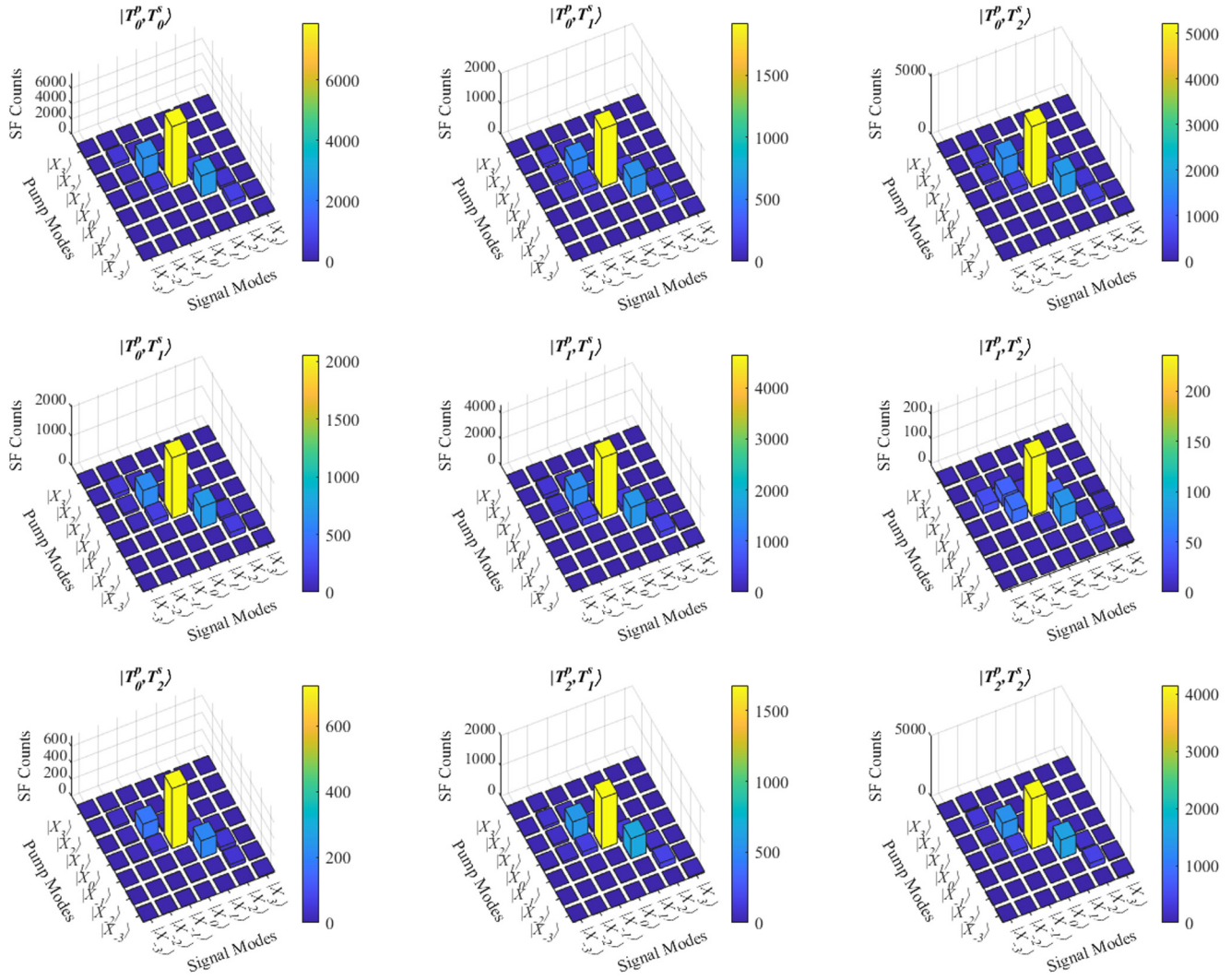

FIG. 5. Measured SF photon counts with different combinations of ST tomography. Here, each of the nine subfigures has a different combination of temporal HG pump and signal modes ($|T_0\rangle$, $|T_1\rangle$ and $|T_2\rangle$) with 7-ps pulse width. Each subfigure consists of SF counts data corresponding to 25 combinations of spatial LG pump and signal modes ($|X_{-3}\rangle$, $|X_{-2}\rangle$, $|X_{-1}\rangle$, $|X_0\rangle$, $|X_1\rangle|X_2\rangle$, and $|X_3\rangle$). The color bar in each subfigure represents the SF photon counts.

each combination of the pump and signal temporal mode, we observe the trend of SF photon counts for a combination of different spatial modes, ranging from $|X_{-3}\rangle$ through $|X_3\rangle$. Among the nine subplots, we observe that the diagonal elements have the highest SF count due to having identical temporal modes. Also, within each subplot, we notice a similar trend where the diagonal elements corresponding to $|X_i\rangle|X_{-i}\rangle$ have a higher SF count as compared to the off-diagonal elements.

Selectivity of superposed modes: it has been shown that encoding information in higher dimensions like arbitrary superpositions of single-photon temporal modes can significantly increase the security of the QKD protocol [23,30,45,59]. Here, we consider two additional modes in MUB by superposing two orthogonal temporal modes $|T_0\rangle$ and $|T_1\rangle$:

$$|T_+\rangle = \frac{1}{\sqrt{2}}(|T_0\rangle + |T_1\rangle), \tag{3}$$

$$|T_-\rangle = \frac{1}{\sqrt{2}}(|T_0\rangle - |T_1\rangle). \tag{4}$$

In Table III, we show the selectivity results for these superposed modes by utilizing optimized and unoptimized pump pulses with a temporal width of 2 and 7 ps. It shows that we can pick individual superposed mode $|T^s_+\rangle$ ($|T^s_-\rangle$) against $|T^s_-\rangle$ ($|T^s_+\rangle$) and $|T^s_2\rangle$ modes with high selectivity. Similarly, $|T^s_2\rangle$ can be selected against $|T^s_+\rangle$ and $|T^s_-\rangle$. The selectivity can be further improved in all three cases by

TABLE III. Experimentally recorded temporal mode selectivity results using superposed signal modes $|T^s_+\rangle$, $|T^s_-\rangle$, and mode 3 ($|T^s_2\rangle$) with temporally optimized and unoptimized pump mode $|T^p_+\rangle$, $|T^p_-\rangle$, and mode 3 ($|T^p_2\rangle$) for two different pulse widths in a 2.5-cm-long crystal. The selectivity values are similarly calculated using Eq. (1).

Pump mode	Pulse width (ps)	$\|T^s_+\rangle$ (dB)	$\|T^s_-\rangle$ (dB)	$\|T^s_2\rangle$ (dB)	Pulse width (ps)	$\|T^s_+\rangle$ (dB)	$\|T^s_-\rangle$ (dB)	$\|T^s_2\rangle$ (dB)
$\|T^p_+\rangle$	2	9.17	−13.54	−11.54	7	7.81	−11.37	−10.98
$\|T^p_-\rangle$	2	−16.20	10.61	−12.23	7	−13.43	8.65	−10.81
$\|T^p_2\rangle$	2	−8.17	−9.19	5.04	7	−7.47	−7.23	3.46
Optimized $\|T^p_+\rangle$	2	13.41	−20.83	−14.35	7	10.16	−16.91	−11.37
Optimized $\|T^p_-\rangle$	2	−16.38	11.67	−13.67	7	−17.31	10.79	−12.06
Optimized $\|T^p_2\rangle$	2	−10.74	−11.45	7.72	7	−8.31	−5.54	2.75

optimizing the pump pulses numerically. As the model section explains, we use the PSO technique to optimize the pump pulses numerically. For 2-ps temporal pulses, we observe an increase in selectivity from 22.71 to 34.24 dB for mode $|T^p_+\rangle$, 26.8 to 28.05 dB for mode $|T^p_-\rangle$, and 14.23 to 19.17 dB for mode $|T^p_2\rangle$. Similarly, for 7-ps temporal pulses, the selectivity improves from 19.18 to 27.07 dB for mode $|T^p_+\rangle$, 22.08 to 28.1 dB for mode $|T^p_-\rangle$, and 10.69 to 11.06 dB for mode $|T^p_2\rangle$.

V. DISCUSSION

In principle, ST quantum states can form an infinite Hilbert space, increasing a single photon's information

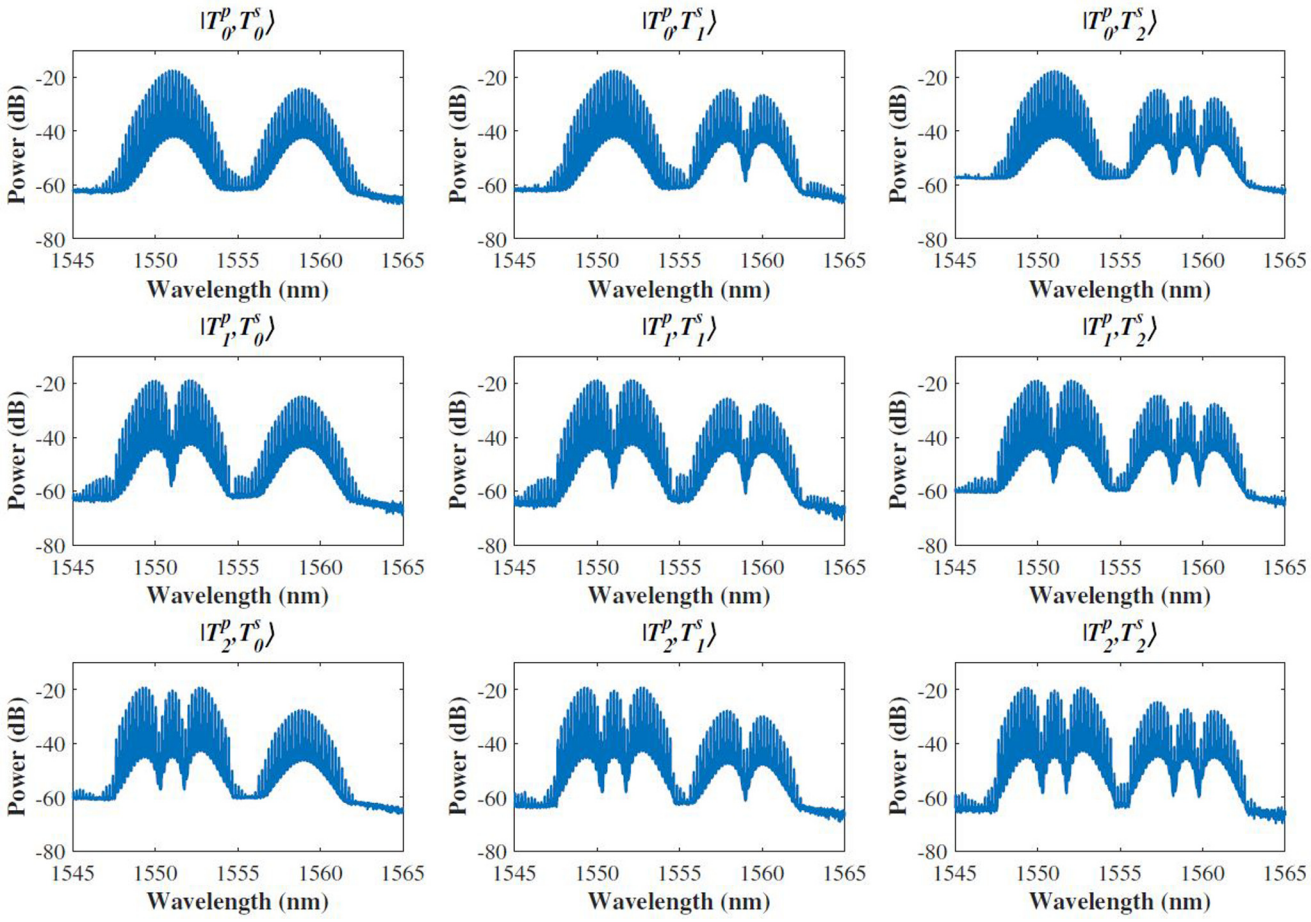

FIG. 6. 2-ps temporal pump and signal profiles in the spectral domain as read by an optical spectrum analyzer after 13-dB attenuation. The central wavelength of the pump and signal are 1551 and 1559 nm, respectively.

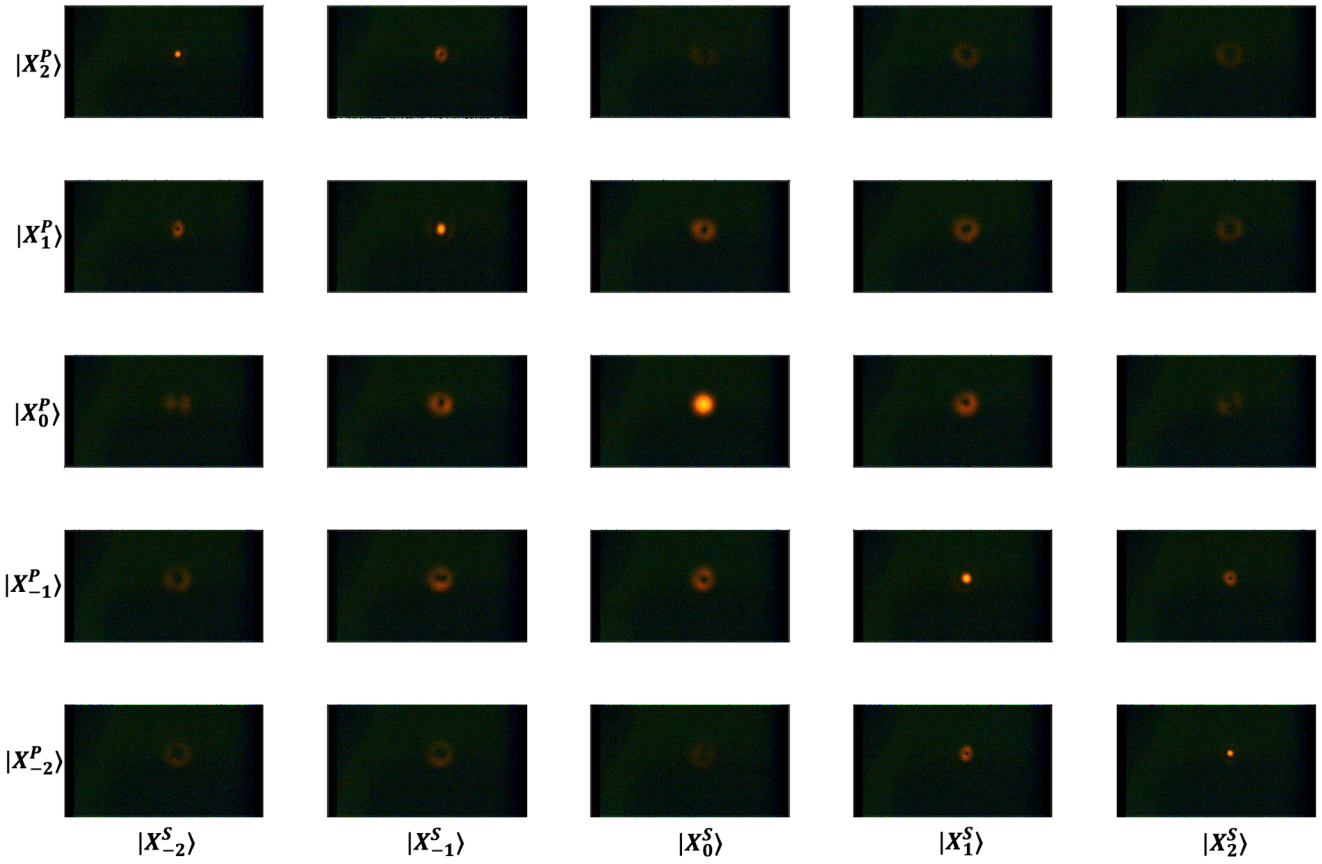

FIG. 7. Experimentally measured spatial profiles of SF output, detected on a CCD camera (for classical measurement), using different sets of signal ($|X^S_{\{i\equiv 0,\pm 1,\pm 2\}}\rangle$) and pump ($|X^P_{\{i\equiv 0,\pm 1,\pm 2\}}\rangle$) modes.

capacity. Convenience in encoding and decoding quantum information in these ST Hilbert spaces can make it beneficial for achieving enhanced key rates for HD quantum key distribution. In this work, we prepare quantum states in a unique set of spatial and temporal modes by combining a SLM, an OFCG, and a waveshaper. We demonstrate a programmable quantum parametric mode sorter to pick the desired ST mode with high selectivity using the SF process in a χ^2 nonlinear crystal. We can achieve between 12.99 to 19.4 dB selectivity among two overlapping spatial modes and between 10.77 to 21.52 dB selectivity among two overlapping temporal modes. We can further improve this up to approximately 26.67 dB by optimizing temporal pump modes.

In our system, there are some technical limitations. For instance, in generating higher-order spatial and temporal quantum states. To create ultrafast pulses in the temporal domain, we use OFCG with a line spacing of 25 GHz (spectral spacing 0.2 nm) limits the effective number of comb lines used for pulse shaping. For a 2-ps pulse, the spectral FWHM is 1.6 nm, which means that we effectively have eight comb lines in the 3-dB bandwidth range, this is inadequate to realize modes higher than third order. Similarly, the higher-order modes in the spatial domain with opposite orbital angular momentum for signal and pump give low photon counts after coupling into the single mode fiber (approximately 4-μm core diameter). This can be seen in the diagonal elements of Figs. 4 and 5. Replacing single-mode fiber with few-mode fiber could help us couple higher-order OAM quantum states [60,61] but the spatial selectivity would be compromised.

In the current setup, we generate ultrafast picosecond level temporal pulses by individually manipulating the phase of 37 optical frequency comb lines using a Finisar waveshaper. We find that when the phase patterns are refreshed in the waveshaper, it introduces a temporal jitter of approximately 2 ps, which can disturb the temporal overlap between pump and signal input pulses within the crystal. We overcame this issue by scanning the SF counts for the different delays between the pump and the signal using an optical delay line. Since this is in excellent agreement with the simulation results, we are able to overlap them and measure the counts at the complete intersections between the input pulses. Our delay and SF count measurement for each pair of pump and signal modes roughly take about 1 s in our MATLAB-based interface. This, though fast enough for the initial assembling of the system, could be a substantial hindrance when it comes to adaptively

optimizing the temporal shape of the pump by using the SF photon counts as feedback. However, it may be possible to achieve a higher selectivity by adaptively optimizing the temporal pump pulse at the cost of increased operation time.

An on-demand single-photon source is vital for most quantum technological applications because of its negligibly low jitter, high spectral purity, and high collection efficiency. In quantum optics experiments, spontaneous parametric down-conversion is commonly used as a heralded single-photon source since we can tailor the joint spectral amplitude function to control the temporal mode structure of the generated photon pair [62–64]. However, multiphoton pair generation reduces the purity of the single photons and can lead to errors in the operation of quantum circuits. One way to reduce the generation of these multiphotons is by weakly pumping the nonlinear crystal, on the other hand, reduces the mean photon number and leads to a lower probability of single-photon output. We can overcome this inherent inefficiency of the heralded single photons produced in a SPDC crystal by selectively up-converting the output heralded and heralding single photons by using two identical quantum parametric mode sorters [43], as described in this paper, to achieve a single-photon source with a highly diminished mode mismatch. We can also use photon-number-resolving detectors to monitor the number of photon pairs per pulse and select only those cases for which only one pair is generated, and further ensure the purity of the shaped single photons [65,66]. To beneficially utilize the enormous information capacity of a single photon in a HD ST Hilbert space, individual ST modes can be extracted by cascading the current QPMS scheme in a serial or loop structure [56,67–69]. We can further optimize the temporal and spatial tomography of the pump in the present QPMS scheme to mitigate both the effect of atmospheric turbulence on the OAM states [38,59,70] and the effect of broadband noise overlapping in the spectral and temporal domain [42].

VI. CONCLUSION

In summary, we develop a fully programmable quantum parametric mode sorter on a combined ST mode basis. By utilizing the optimized pump modes, coupling into the single-mode fiber, and operating at the edge of the phase matching in a nonlinear crystal, we show the effective mode-sorting performance in the HD ST Hilbert space. Only optimizing pumps in the temporal domain can achieve more than 12-dB extinction for MUB sets of ST modes. This technique could find applications in HD quantum communications and computations, quantum cryptography, pattern recognition, and quantum LiDAR [46,71–73], and so on. In the future, we can extend our HD quantum mode-sorting approach for more practical scenarios, such as passing through a noisy environment due to spatial turbulence [38] and/or time-frequency noises [42], which could overlap with the desired signal modes.

FUNDING

This research is supported by the NSF and Earth Science Technology Office, NASA.

DISCLOSURES

The authors declare no conflicts of interest.

ACKNOWLEDGMENTS

The authors thank Jeevanandha Ramanathan for helping with the FPGA-based photon-counting system and Bhavya Mohan for helping with the three-dimensional diagram of the experimental setup.

APPENDIX A

Spectral profiles of 2-ps temporal pulses: we generate ultrafast temporal pulses by individually manipulating the phase and amplitude of optical frequency comb lines generated by an OFCG. We combine 5% of pump and signal pulses using a beam combiner to observe them in the spectral domain using an OSA. In Fig. 6, we show the spectral profiles of different pump and signal modes with center wavelengths 1551 and 1559 nm. We observe a slight power at the phase-matching wavelength for second-harmonic generation (approximately 1555 nm), which gives rise to considerable noise photon counts in a single-photon regime. To avoid this, we further use free-space short-pass and long-pass filters on the signal and pump arm, respectively.

APPENDIX B

Camera image of spatial modes: to verify the profile of the spatial modes, we experimentally capture the classical SF output on a CCD camera as shown in Fig. 7. The spatial intensity profile of the SF output for the combination of $|X^p_{-2}\rangle$, $|X^p_{-1}\rangle$, $|X^p_0\rangle$, $|X^p_1\rangle$, and $|X^p_2\rangle$ pump modes with $|X^s_{-2}\rangle$, $|X^s_{-1}\rangle$, $|X^s_0\rangle$, $|X^s_1\rangle$, and $|X^s_2\rangle$ signal modes are in excellent agreement with the simulated results shown in Fig. 1(v).

TABLE IV. Three different temporal pulse widths are used to experimentally evaluate the mode selection of signal mode 1 (HG_{00}) and 2 (HG_{01}) with temporally optimized and unoptimized pumps using 1-cm crystal.

Pulse width (ps)	$\|T^p_0\rangle$ (dB)	Optimized $\|T^p_0\rangle$ (dB)	$\|T^p_1\rangle$ (dB)	Optimized $\|T^p_1\rangle$ (dB)
1	8.03	11.1	7.6	8.1
2	6.26	9.5 dB	4.5	4.5
3	5.0	8.2	2.74	4.4

APPENDIX C

QPMS and temporal walkoff: Table IV, illustrates how mode selectivity is influenced by the temporal walkoff between the pump and SF pulses in the crystal. Signal modes $|T_0\rangle$ and $|T_1\rangle$ are selectively up-converted using a temporally optimized and unoptimized pump pulse in a 1-cm crystal. We show a sudden drop in the selectivity beyond a temporal pulse width of 1 ps since the temporal walkoff between the pump and SF pulses in the crystal is approximately 1.2 ps. Though there is a drop in selectivity between 2- and 3-ps pulses, they are comparable to each other.

[1] M. O. Scully and M. S. Zubairy, *Quantum Optics* (Cambridge University Press, Cambridge, 1997).

[2] C. Couteau, Spontaneous parametric down-conversion, Contemp. Phys. **59**, 291 (2018).

[3] E. Rozenberg, A. Karnieli, O. Yesharim, J. Foley-Comer, S. Trajtenberg-Mills, D. Freedman, A. M. Bronstein, and A. Arie, Inverse design of spontaneous parametric downconversion for generation of high-dimensional qudits, Optica **9**, 602 (2022).

[4] J.-Y. Chen, Z.-H. Ma, Y. M. Sua, Z. Li, C. Tang, and Y.-P. Huang, Ultra-efficient frequency conversion in quasi-phase-matched lithium niobate microrings, Optica **6**, 1244 (2019).

[5] X. Lu, G. Moille, Q. Li, D. A. Westly, A. Singh, A. Rao, S.-P. Yu, T. C. Briles, S. B. Papp, and K. Srinivasan, Efficient telecom-to-visible spectral translation through ultralow power nonlinear nanophotonics, Nat. Photon. **13**, 593 (2019).

[6] R. Ghosh and L. Mandel, Observation of Nonclassical Effects in the Interference of Two Photons, Phys. Rev. Lett. **59**, 1903 (1987).

[7] P. Kumar, Quantum frequency conversion, Opt. Lett. **15**, 1476 (1990).

[8] A. Hochrainer, M. Lahiri, M. Erhard, M. Krenn, and A. Zeilinger, Quantum indistinguishability by path identity and with undetected photons, Rev. Mod. Phys. **94**, 025007 (2022).

[9] J. Wang, Y.-F. Huang, C. Zhang, J.-M. Cui, Z.-Y. Zhou, B.-H. Liu, Z.-Q. Zhou, J.-S. Tang, C.-F. Li, and G.-C. Guo, Universal Photonic Quantum Interface for a Quantum Network, Phys. Rev. Appl. **10**, 054036 (2018).

[10] K. Niizeki, D. Yoshida, K. Ito, I. Nakamura, N. Takei, K. Okamura, M.-Y. Zheng, X.-P. Xie, and T. Horikiri, Two-photon comb with wavelength conversion and 20-km distribution for quantum communication, Commun. Phys. **3**, 138 (2020).

[11] B. Albrecht, P. Farrera, X. Fernandez-Gonzalvo, M. Cristiani, and H. de Riedmatten, A waveguide frequency converter connecting rubidium-based quantum memories to the telecom c-band, Nat. Commun. **5**, 3376 (2014).

[12] M. Bock, P. Eich, S. Kucera, M. Kreis, A. Lenhard, C. Becher, and J. Eschner, High-fidelity entanglement between a trapped ion and a telecom photon via quantum frequency conversion, Nat. Commun. **9**, 1998 (2018).

[13] J. S. Dam, P. Tidemand-Lichtenberg, and C. Pedersen, Room-temperature mid-infrared single-photon spectral imaging, Nat. Photon. **6**, 788 (2012).

[14] N. M. Israelsen, P. J. Rodrigo, C. R. Petersen, G. Woyessa, R. E. Hansen, P. Tidemand-Lichtenberg, C. Pedersen, and O. Bang, High-resolution mid-infrared optical coherence tomography with kHz line rate, Opt. Lett. **46**, 4558 (2021).

[15] K. Huang, J. Fang, M. Yan, E. Wu, and H. Zeng, Wide-field mid-infrared single-photon upconversion imaging, Nat. Commun. **13**, 1077 (2022).

[16] C. Senko, P. Richerme, J. Smith, A. Lee, I. Cohen, A. Retzker, and C. Monroe, Realization of a Quantum Integer-Spin Chain with Controllable Interactions, Phys. Rev. X **5**, 021026 (2015).

[17] B. Yan, S. A. Moses, B. Gadway, J. P. Covey, K. R. A. Hazzard, A. M. Rey, D. S. Jin, and J. Ye, Observation of dipolar spin-exchange interactions with lattice-confined polar molecules, Nature **501**, 521 (2013).

[18] V. Parigi, V. D'Ambrosio, C. Arnold, L. Marrucci, F. Sciarrino, and J. Laurat, Storage and retrieval of vector beams of light in a multiple-degree-of-freedom quantum memory, Nat. Commun. **6**, 7706 (2015).

[19] M. Neeley, M. Ansmann, R. C. Bialczak, M. Hofheinz, E. Lucero, A. D. O'Connell, D. Sank, H. Wang, J. Wenner, A. N. Cleland, M. R. Geller, and J. M. Martinis, Emulation of a quantum spin with a superconducting phase qudit, Science **325**, 722 (2009).

[20] X.-L. Wang, X.-D. Cai, Z.-E. Su, M.-C. Chen, D. Wu, L. Li, N.-L. Liu, C.-Y. Lu, and J.-W. Pan, Quantum teleportation of multiple degrees of freedom of a single photon, Nature **518**, 516 (2015).

[21] B. Brecht, D. V. Reddy, C. Silberhorn, and M. G. Raymer, Photon Temporal Modes: A Complete Framework for Quantum Information Science, Phys. Rev. X **5**, 041017 (2015).

[22] P. Boucher, C. Fabre, G. Labroille, and N. Treps, Spatial optical mode demultiplexing as a practical tool for optimal transverse distance estimation, Optica **7**, 1621 (2020).

[23] M. Plöschner, M. M. Morote, D. S. Dahl, M. Mounaix, G. Light, A. D. Rakić, and J. Carpenter, Spatial tomography of light resolved in time, spectrum, and polarisation, Nat. Commun. **13**, 4294 (2022).

[24] L. G. Wright, W. H. Renninger, D. N. Christodoulides, and F. W. Wise, Nonlinear multimode photonics: Nonlinear optics with many degrees of freedom, Optica **9**, 824 (2022).

[25] C. He, Y. Shen, and A. Forbes, Towards higher-dimensional structured light, Light: Sci. Appl. **11**, 205 (2022).

[26] S. C. Yorulmaz, M. P. van Exter, and M. J. A. de Dood, The role of spatial and temporal modes in pulsed parametric down-conversion, Opt. Express **22**, 5913 (2014).

[27] M. Erhard, R. Fickler, M. Krenn, and A. Zeilinger, Twisted photons: New quantum perspectives in high dimensions, Light: Sci. Appl. **7**, 17146 (2018).

[28] M. G. Raymer and K. Banaszek, Time-frequency optical filtering: efficiency vs. temporal-mode discrimination in incoherent and coherent implementations, Opt. Express **28**, 32819 (2020).

[29] E. Otte, I. Nape, C. Rosales-Guzmán, C. Denz, A. Forbes, and B. Ndagano, High-dimensional cryptography with

spatial modes of light: Tutorial, J. Opt. Soc. Am. B **37**, A309 (2020).
[30] J. L. Habif, A. Jagannathan, S. Gartenstein, P. Amory, and S. Guha, Quantum-limited discrimination of laser light and thermal light, Opt. Express **29**, 7418 (2021).
[31] V. Ansari, B. Brecht, J. Gil-Lopez, J. M. Donohue, J. Řeháček, Z. c. v. Hradil, L. L. Sánchez-Soto, and C. Silberhorn, Achieving the Ultimate Quantum Timing Resolution, PRX Quantum **2**, 010301 (2021).
[32] G. S. Thekkadath, B. A. Bell, R. B. Patel, M. S. Kim, and I. A. Walmsley, Measuring the Joint Spectral Mode of Photon Pairs using Intensity Interferometry, Phys. Rev. Lett. **128**, 023601 (2022).
[33] S. Xu, H. Z. Shen, and X. X. Yi, Demultiplexing of photonic temporal modes by a linear system, Phys. Rev. A **97**, 033841 (2018).
[34] S. Wei, S. K. Earl, J. Lin, S. S. Kou, and X.-C. Yuan, Active sorting of orbital angular momentum states of light with a cascaded tunable resonator, Light: Sci. Appl. **9**, 10 (2020).
[35] A. Mair, A. Vaziri, G. Weihs, and A. Zeilinger, Entanglement of the orbital angular momentum states of photons, Nature **412**, 313 (2001).
[36] G. C. G. Berkhout, M. P. J. Lavery, J. Courtial, M. W. Beijersbergen, and M. J. Padgett, Efficient Sorting of Orbital Angular Momentum States of Light, Phys. Rev. Lett. **105**, 153601 (2010).
[37] N. K. Fontaine, R. Ryf, H. Chen, D. T. Neilson, K. Kim, and J. Carpenter, Laguerre-Gaussian mode sorter, Nat. Commun. **10**, 1865 (2019).
[38] H. Zhang, S. Kumar, and Y.-P. Huang, Mode selective upconversion detection with turbulence, Sci. Rep. **9**, 17481 (2019).
[39] H. Defienne and D. Faccio, Arbitrary spatial mode sorting in a multimode fiber, Phys. Rev. A **101**, 063830 (2020).
[40] J. Pinnell, I. Nape, B. Sephton, M. A. Cox, V. Rodríguez-Fajardo, and A. Forbes, Modal analysis of structured light with spatial light modulators: A practical tutorial, J. Opt. Soc. Am. A **37**, C146 (2020).
[41] A. Eckstein, B. Brecht, and C. Silberhorn, A quantum pulse gate based on spectrally engineered sum frequency generation, Opt. Express **19**, 13770 (2011).
[42] A. Shahverdi, Y. M. Sua, L. Tumeh, and Y.-P. Huang, Quantum parametric mode sorting: Beating the time-frequency filtering, Sci. Rep. **7**, 6495 (2017).
[43] D. V. Reddy, M. G. Raymer, C. J. McKinstrie, L. Mejling, and K. Rottwitt, Temporal mode selectivity by frequency conversion in second-order nonlinear optical waveguides, Opt. Express **21**, 13840 (2013).
[44] K. G. Köprülü, Y.-P. Huang, G. A. Barbosa, and P. Kumar, Lossless single-photon shaping via heralding, Opt. Lett. **36**, 1674 (2011).
[45] P. Manurkar, N. Jain, M. Silver, Y.-P. Huang, C. Langrock, M. M. Fejer, P. Kumar, and G. S. Kanter, Multidimensional mode-separable frequency conversion for high-speed quantum communication, Optica **3**, 1300 (2016).
[46] F. Devaux, A. Mosset, P.-A. Moreau, and E. Lantz, Imaging Spatiotemporal Hong-Ou-Mandel Interference of Biphoton States of Extremely High Schmidt Number, Phys. Rev. X **10**, 031031 (2020).
[47] M. G. Raymer and I. A. Walmsley, Temporal modes in quantum optics: Then and now, Phys. Scr. **95**, 064002 (2020).
[48] S. Kumar, H. Zhang, P. Kumar, M. Garikapati, Y. M. Sua, and Y.-P. Huang, Spatiotemporal mode-selective quantum frequency converter, Phys. Rev. A **104**, 023506 (2021).
[49] S. Kumar, H. Zhang, S. Maruca, and Y.-P. Huang, Mode-selective image upconversion, Opt. Lett. **44**, 98 (2019).
[50] A. Pe'er, B. Dayan, A. A. Friesem, and Y. Silberberg, Temporal Shaping of Entangled Photons, Phys. Rev. Lett. **94**, 073601 (2005).
[51] Z. Jiang, C.-B. Huang, D. E. Leaird, A. M. Weiner, M. Kourogi, and K. Imai, in *Conference on Lasers and Electro-Optics/Quantum Electronics and Laser Science Conference and Photonic Applications Systems Technologies* (Optica Publishing Group, 2007), p. CTuJ3.
[52] D. Cruz-Delgado, S. Yerolatsitis, N. K. Fontaine, D. N. Christodoulides, R. Amezcua-Correa, and M. A. Bandres, Synthesis of ultrafast wavepackets with tailored spatiotemporal properties, Nat. Photon. **16**, 686 (2022).
[53] S. Clemmen, K. P. Huy, W. Bogaerts, R. G. Baets, P. Emplit, and S. Massar, Continuous wave photon pair generation in silicon-on-insulator waveguides and ring resonators, Opt. Express **17**, 16558 (2009).
[54] J. E. Sharping, K. F. Lee, M. A. Foster, A. C. Turner, B. S. Schmidt, M. Lipson, A. L. Gaeta, and P. Kumar, Generation of correlated photons in nanoscale silicon waveguides, Opt. Express **14**, 12388 (2006).
[55] F. M. Miatto, H. D. L. Pires, S. M. Barnett, and M. P. van Exter, Spatial Schmidt modes generated in parametric down-conversion, Eur. Phys. J. D 66, 263 (2012). ArXiv:1201.3041,
[56] Y.-P. Huang and P. Kumar, Mode-resolved photon counting via cascaded quantum frequency conversion, Opt. Lett. **38**, 468 (2013).
[57] C. Santori, D. Fattal, J. Vučković, G. S. Solomon, and Y. Yamamoto, in *Conference on Lasers and Electro-Optics/Quantum Electronics and Laser Science Conference* (Optica Publishing Group, 2003), p. QME3.
[58] G. Cui and M. G. Raymer, Quantum efficiency of single-photon sources in the cavity-QED strong-coupling regime, Opt. Express **13**, 9660 (2005).
[59] Z. Tao, Y. Ren, A. Abdukirim, S. Liu, and R. Rao, Mitigating the effect of atmospheric turbulence on orbital angular momentum-based quantum key distribution using real-time adaptive optics with phase unwrapping, Opt. Express **29**, 31078 (2021).
[60] D. Cozzolino, D. Bacco, B. Da Lio, K. Ingerslev, Y. Ding, K. Dalgaard, P. Kristensen, M. Galili, K. Rottwitt, S. Ramachandran, and L. K. Oxenløwe, Orbital Angular Momentum States Enabling Fiber-Based High-Dimensional Quantum Communication, Phys. Rev. Appl. **11**, 064058 (2019).
[61] I. Cristiani, *et al.*, Roadmap on multimode photonics, J. Opt. **24**, 083001 (2022).
[62] V. Ansari, G. Harder, M. Allgaier, B. Brecht, and C. Silberhorn, Temporal-mode measurement tomography of a quantum pulse gate, Phys. Rev. A **96**, 063817 (2017).

[63] V. Ansari, J. M. Donohue, B. Brecht, and C. Silberhorn, Tailoring nonlinear processes for quantum optics with pulsed temporal-mode encodings, Optica **5**, 534 (2018).
[64] V. Ansari, J. M. Donohue, B. Brecht, and C. Silberhorn, Remotely projecting states of photonic temporal modes, Opt. Express **28**, 28295 (2020).
[65] T. Kiyohara, R. Okamoto, and S. Takeuchi, Realization of multiplexing of heralded single photon sources using photon number resolving detectors, Opt. Express **24**, 27288 (2016).
[66] D. Bonneau, G. J. Mendoza, J. L. O'Brien, and M. G. Thompson, Effect of loss on multiplexed single-photon sources, New J. Phys. **17**, 043057 (2015).
[67] N. Sangouard, B. Sanguinetti, N. Curtz, N. Gisin, R. Thew, and H. Zbinden, Faithful Entanglement Swapping Based on Sum-Frequency Generation, Phys. Rev. Lett. **106**, 120403 (2011).
[68] D. L. P. Vitullo, M. G. Raymer, B. J. Smith, M. Karpiński, L. Mejling, and K. Rottwitt, Entanglement swapping for generation of heralded time-frequency-entangled photon pairs, Phys. Rev. A **98**, 023836 (2018).
[69] F. Kaneda, J. Oikawa, M. Yabuno, F. China, S. Miki, H. Terai, Y. Mitsumori, and K. Edamatsu, Spectral characterization of photon-pair sources via classical sum-frequency generation, Opt. Express **28**, 38993 (2020).
[70] T. Brünner and F. S. Roux, Robust entangled qutrit states in atmospheric turbulence, New J. Phys. **15**, 063005 (2013).
[71] P. Rehain, Y. M. Sua, S. Zhu, I. Dickson, B. Muthuswamy, J. Ramanathan, A. Shahverdi, and Y.-P. Huang, Noise-tolerant single photon sensitive three-dimensional imager, Nat. Commun. **11**, 921 (2020).
[72] A. Shahverdi, Y. M. Sua, I. Dickson, M. Garikapati, and Y.-P. Huang, Mode selective up-conversion detection for LIDAR applications, Opt. Express **26**, 15914 (2018).
[73] S. Zhu, Y. M. Sua, Y. Hu, C. Weimer, Z. Ma, Z. Zheng, P. Rehain, K. Stamnes, Y. Zhou, J. H. Lee, and Y.-P. Huang, Quantum parametric mode sorting: A case study on small angle scattering, J. Opt. Soc. Am. B **38**, D15 (2021).